24-087

Thermal Runaway Pressures as a Function of Free Space in Sealed Containers for Lithium Titanate Cells

Connor B. Brown, Thomas H. Dubaniewicz, Teresa Barone, and Richard A. Thomas
Pittsburgh Mining Research Division, National Institute for Occupational Safety and Health, Pittsburgh, USA

ABSTRACT

Electric vehicles powered by lithium-ion (Li-ion) batteries are being developed by mining vehicle manufacturers as a replacement for diesel-powered vehicles. Explosion-proof (XP) enclosures are frequently employed to enclose electrical ignition sources in gaseous underground mines to prevent the spread of an internal methane-air explosion to a nearby explosive atmosphere. Due to thermal runaway (TR), Li-ion batteries have the potential to cause pressurized explosions in an enclosed structure. Past research has shown the potential for well-confined Li-ion cell TR to drive pressures beyond the conventional pressure specification for XP enclosures. Researchers at the National Institute for Occupational Safety and Health (NIOSH) used an Accelerating Rate Calorimeter (ARC) to induce thermal runaway of Lithium Titanate or Lithium Titanium Oxide (LTO) type 18650 cells enclosed within containers with various volumes and found an inverse power relationship between the TR pressure and available free space. The results were similar in magnitude to that of lithium iron phosphate (LFP) cells, which were used in prior testing. Temperatures, gas amounts, and TR pressure-rise rates were also recorded. The data indicate that with enough free space, the pressures can be lowered below the conventional pressure specification for XP enclosures.

INTRODUCTION

It has been known that the use of diesel-powered equipment results in generating diesel particulate matter (DPM) which is a known carcinogen [1]. Past NIOSH research has shown that underground mineworkers are at particular risk of DPM exposure [2]. Mine operators can attempt to mitigate this risk by providing enough ventilation to dilute the DPM below safe limits. The hierarchy of controls dictates the elimination of the DPM source as the best way to control the risk. For this reason, among others, mine vehicle manufacturers are developing battery electric vehicle (BEV) versions of their current equipment. Due to their high energy density, lithium-ion batteries (LIB) are one of the most common choices for manufacturers of BEVs when they transition away from diesel-powered vehicles [3]. Due to the high energy demands in mining, BEVs utilize a vast number of individual battery cells wired in series and parallel to achieve the necessary voltage and current requirements, normally in the range of hundreds of kilowatt-hours of capacity.

In the consumer sector, there have been several accidents involving a Li-ion battery in everything from small portable devices to large commuter transports to entire cargo ships [4–6]. Events of LIB failures in mines have also occurred [7 & 8]. Accidents of lithium-ion battery TR in mines will become more prominent and more ubiquitous

Table 1. Summary of LIB cell characteristic

Type	LTO	LFP		NMC
Size	18650	18650	26650	18650
Voltage, V	2.4	3.2	3.2	3.67
Capacity, Ah	1.3	1.5	3.8	3.2
Energy, Wh	3.1	4.8	12.2	11.7
Approx. cell weight, g	38	41	88	45
Energy density, Wh/kg	82	117	138	260

as the use the BEVs and wearable equipment continue to be more commonplace. The challenges are compounded in applications that implement large banks of LIB. The main cause of the catastrophic failure of LIB is a thermal runway, which happens when the heat generated by the exothermic reaction outpaces the heat dissipated by the battery which leads to increased reaction rates, temperatures, and pressures. If no mitigation efforts are made, the accelerating self-reinforcing process will lead to the venting of toxic and flammable gases and elevated temperature and in turn fires and explosions [9]. The initial TR can be caused by many internal or external factors such as internal shorts, mechanical damage, exposure to heat, surging currents, and faulty wiring. The severity of these failures is also dependent on the discharge rate, state of charge, and internal chemistries of the LIB (cathode anode, electrolyte, separator) [10]. Large equipment powered by LIB has the additional risk of a cascade of thermal runaways caused by a single battery cell in TR and generating enough heat to drive the neighboring batteries to catastrophic failure. Explosion-proof enclosures are required by the Mine Safety and Health Administration (MSHA) to contain an internal methane-air explosion and stop the propagation of the explosion into the explosible mine atmosphere [11]. The enclosure must be capable of withstanding a minimum pressure of 150 psig (10.3 barg), and the outside surfaces of the XP container are not allowed to reach 150 °C. If any pressure peak exceeds 125 psig, the manufacturer must either conduct static pressure tests on the enclosure to ensure that it can withstand a static pressure twice as high as the highest value recorded in any previous tests or make constructional changes that will lower the pressure to 125 psig or less [12]. Prior testing of other LIB, namely iron phosphate (LFP) and nickel manganese cobalt (NMC), has been conducted in containers of varying volumes. The results of this past NIOSH research showed an inverse power relationship between the peak pressures and the amount of free space within the containers, but due to the inherent variations in the different battery chemistries, it was found that NMC batteries required more than eight times the amount of free space per cell volume than LFP to meet the 125 psig XP enclosure specifications [13, 14]. The current study is a continuation of this previous research in which the composition of the LTO type LIB was characterized and the battery cells were tested in various-sized containers to determine how the specific chemistry influenced the relationship between peak pressure and the amount of free space and how it compares to the other LIB chemistries.

METHODS

The LIB selected for this study were cylindrical spiral-wound type 18650 manufactured by Hua Hui Energy. The cells are the same cells that were studied by Yuan et al. [15] with a nominal voltage and rated capacity of 2.4 V and 1.3 Ah, respectively. Table 1 shows the comparative energy density of LIB cells

The battery cell composition was characterized by scanning electron microscopy (SEM; Model S-4800, Hitachi, Tokyo, Japan) and energy dispersive x-ray spectroscopy (EDS; Bruker Quantax, Madison, Wisconsin). The samples for SEM/EDS analysis were extracted from the cell after fully discharging it for personnel safety and were mounted on 25-mm aluminum posts with conductive carbon tape. The separator was coated with gold and palladium to avoid image distortion from a lack of sample conductivity, while the anode and cathode remained uncoated due to their high conductivity. Particle size was measured with ImageJ software (Version 1.48v, National Institutes of Health).

An Arbin Multi-channel potentiostat/galvanostat (MSTAT, Arbin Instruments, College Station, Texas) was used to cycle the cells through three charge-discharge cycles before bringing the cells to a full state of charge. The measured discharge capacity of the cells was at least 95% of the rated capacity.

The LIB TR tests were conducted using an accelerating rate calorimeter (ARC) (model EV+, Thermal Hazard Technology, Milton Keynes, United Kingdom) (Figure 1) and a stand-alone data acquisition system (model DI-720, DATAQ Instruments, Akron, Ohio) with a faster measurement rate to capture peak thermal runaway pressures.

The testing consisted of placing a fully charged LIB cell and in some cases three LIB cells, which passed the 95% capacity screening, into sealed a container and driving

Figure 1. Accelerating Rate Calorimeter

Figure 2. Containers provided various amounts of free space

them into thermal runaway. Most of the containers were fabricated from schedule 80 steel pipe except for the largest 6-in diameter pipe which used schedule 40. The additional containers include the 1.5-in, 2-in, 2.5-in, 3-in, and 4-in diameter pipes (Figure 2). In addition, an insert was fabricated for the 2-in pipe to accept the size of the 18650 cells and displace additional free space. The internal volumes were measured by filling the containers with water, including the fittings, and pouring out the water into beakers (Table 2).

The threaded caps were drilled and tapped to include compression fittings on the caps to allow for venting gases, measuring pressure and voltage, and inserting thermocouples. One cell was placed within each sealed container per test. In addition, one set of tests used three cells wired in series and placed in a 1,175-ml canister (Figure 3).

N-type thermocouples were placed on the outside wall of the canister, and when enough space was available, they were placed inside the canister to measure the temperature of the gases and the surface temperature of the cell. Several pressure transducers were used from 30 psi to 3,000 psi maximum pressure depending on expected pressures. The thermocouples, battery leads, and a pressure transducer were connected to the ARC system and samples were taken every 0.6 seconds. The pressure transducer connected to the DataQ system met the requirement of the MSHA explosion testing at 100 samples per second. Each set of test conditions was conducted three times, resulting in 24 total

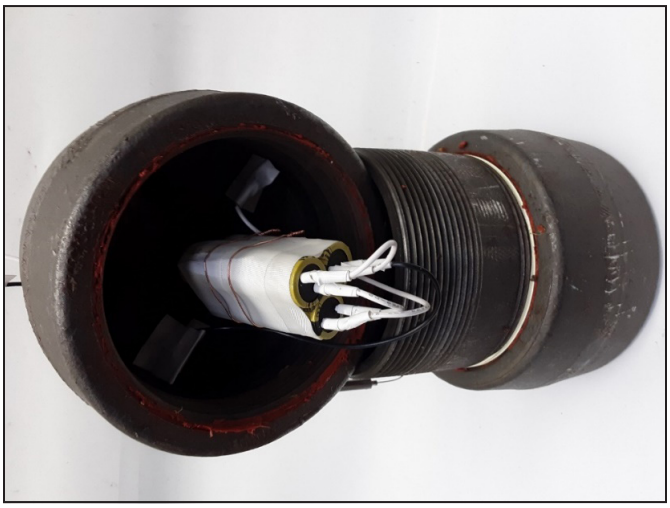

Figure 3. An example of a triple LTO cell test in the 1,175-ml container

tests conducted. A diagram of the test setup is shown in Figure 4.

RESULTS AND DISCUSSION

Cell Composition

The cell was examined to confirm the anode composition specified by the manufacturer and to evaluate other components, including the cathode and separator. The analysis of the anode showed that the major elements were titanium and oxygen (Figure 5a) consistent with the

Table 2. Internal volumes of various canisters

Canister Diameter, in.	1.5	2 + insert	2	2.5	3	4	6
Internal Volume, ml	71	109	185	284	702	1175	2795

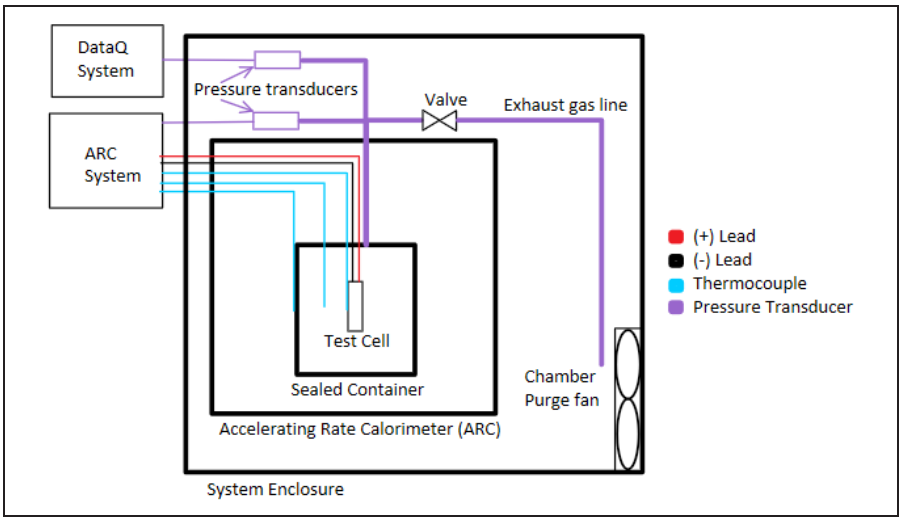

Figure 4. Experimental setup for LTO battery TR Pressure and Volume Study

manufacturer-indicated cell type ($Li_4Ti_5O_{12}$; LTO). (Note: Lithium could not be detected because the SEM was not equipped with a windowless EDS detector that measures very light elements.) This composition is widely used in commercial lithium-ion batteries [17, 18] and is considered to enhance battery safety through its excellent cycling stability. Specifically, this composition does not swell or contract significantly during charging and discharging, which prevents an internal short circuit [19].

A small amount of carbon (Figure 5a) was present in the conductive filler (nanoparticle aggregates) and binder (film covering microparticles) (Figure 6a) of the LTO anode. Carbon fillers may have been incorporated to improve the relatively low electrical conductivity of the LTO anode [20]. Electrical conductivity and ionic conductivity are also enhanced by small LTO particle sizes [19]. The approximate size of the LTO particles in the current study was 420 ±120 nm. This size range was shown to have better electrochemical properties (greater specific capacity and rate capability) than larger particles [21, 22]. Particle size did not substantially influence thermal stability or the ability to resist decomposition at high temperatures [23]. Thermal stability may be more dependent on the cathode than the anode composition [24].

The cathode contained cobalt and manganese in an apparent ratio of 1:1 (Figure 5b) in the Lithium Cobalt Manganese Oxide (LCMO) cells. This composition is much less common than cathodes of nickel, manganese, and cobalt. The LCMO composition has received attention in the last few years due to its potential as a high-voltage (5 V) cathode [25, 26]. However, when the LCMO cathode is paired with an LTO anode, the voltage plateau of the LTO limits the entire cell voltage [20, 27]. An LCMO cathode

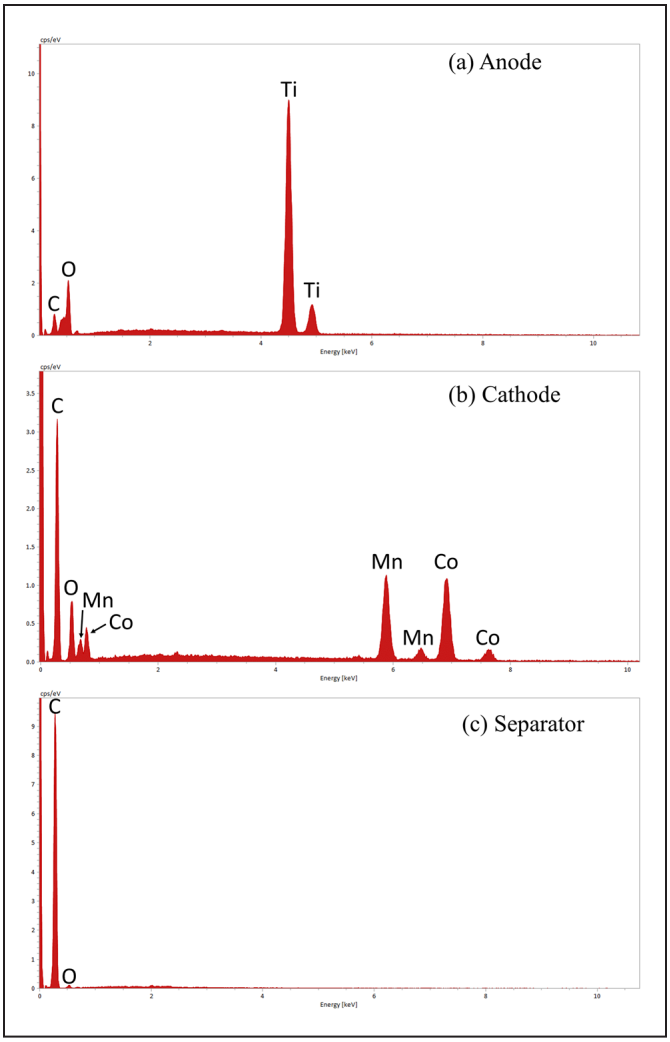

Figure 5. EDS spectra of LTO cell (a) anode, (b) cathode, and (c) separator [16]

may have been used in the current battery due to its excellent safety features. For example, the LCMO cathode has cycling stability that approaches the minimal strain properties of the LTO anode [27]. In addition, it has very high thermal stability—the LCMO cathode withstood temperatures up to 480 °C when paired with the LTO anode and a solid-state (inflammable) electrolyte [28]. Because the LTO and LCMO electrodes are thermally stable, the electrolyte and separator become the main vulnerabilities.

The separator contained mostly carbon (Figure 5c) and had the morphology of a porous polymer membrane (Figure 6c) [29]. Porous polymer membranes have good lithium-ion conductivity, but the organic membrane can fail at high temperatures and can be vulnerable to punctures by lithium dendrites [29, 30]. Overall, the characterization suggests that the separator had a composition with relatively low thermal abuse tolerance but was balanced by a robust anode and cathode.

Temperatures

Figure 7 shows the time plots of the recorded temperatures and cell voltage of a single cell in a 1,175-ml container. The cell temperature was gathered via a thermocouple secured to the outer metal casing of the LTO battery with fiber tape and copper wire. As expected, the container temperature leads the gas temperature which leads the cell temperature during the heating process. It's not until the venting event after 90 minutes that the cell begins a self-heating process where the internal exothermic chemical reactions and internal shorts lead to increasing heat. Around the time of the venting, a small voltage drop is observable. The rate of the drop increases until an internal short causes a thermal runway, possibly due to a thermally degraded polymer separator.

The gas temperature was recorded via a thermocouple hanging in the available free space within the container, and the container thermocouple was secured to the outer body of the sealed steel pipe with glass fiber tape. The maximum recorded temperatures were found to be 161 °C for the gas and 164 °C for the container. In the smaller containers, 109 ml and 71 ml, the gas and cell temperatures were not able to be measured due to the lack of available free space. Figure 8 shows a boxplot of the recorded gas, cell, and container temperature at the peak of recorded pressure rates during venting.

During much of the heating process, the cell temperature lags in both gas and container temperatures. It is not until the cell begins self-heating that the cell temperature climbs past the gas temperature, and in some cases, at the time of venting, exceeds the temperature of the container.

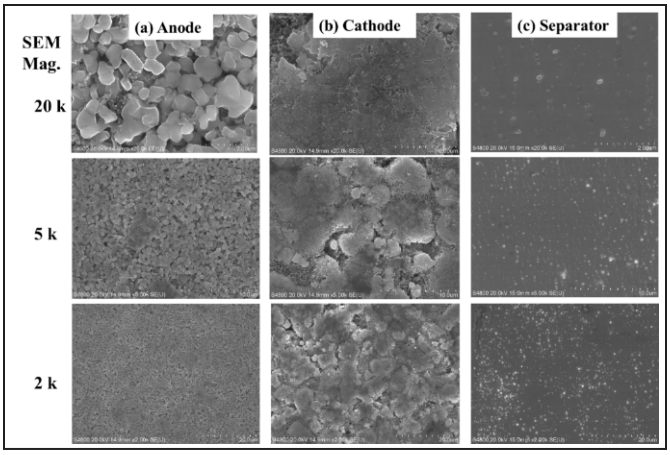

Figure 6. SEM images of the LTO cell (a) anode, (b) cathode, and (c) separator [16]

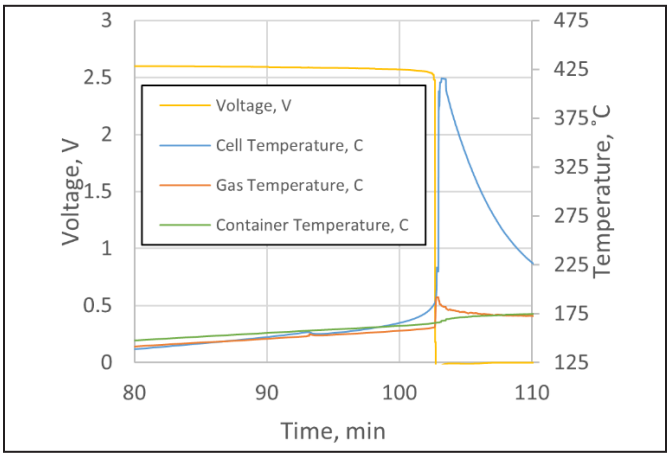

Figure 7. Temperature and voltage plot of LTO-18650 in a 1,175-ml container

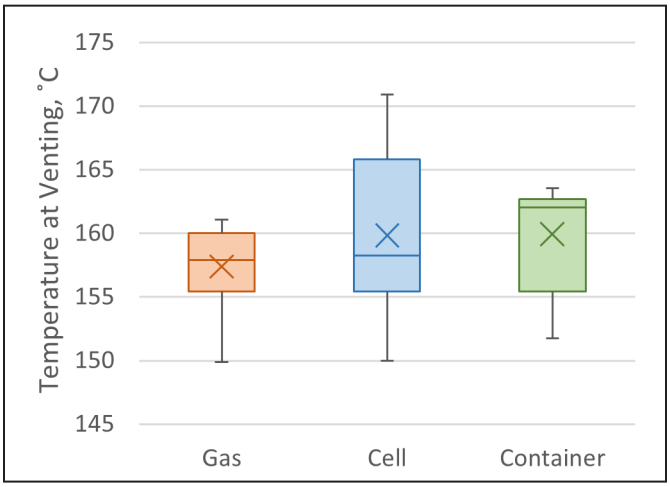

Figure 8. Summary of gas, cell, and container temperatures at venting

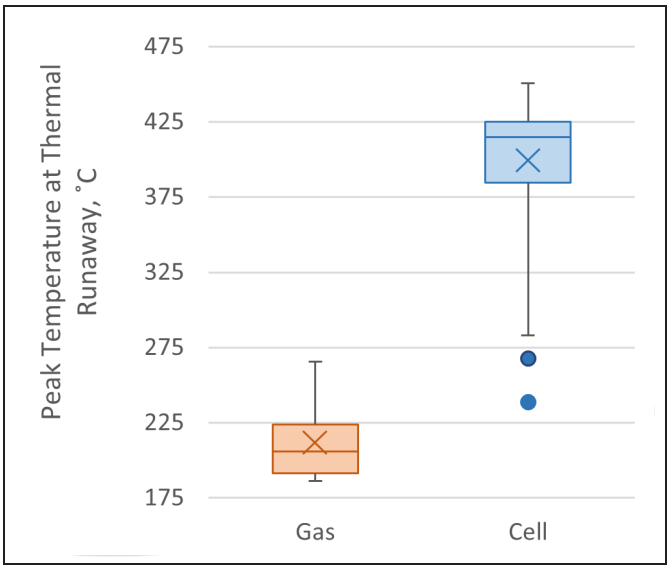

Figure 9. Peak gas and cell temperatures associated with thermal runway

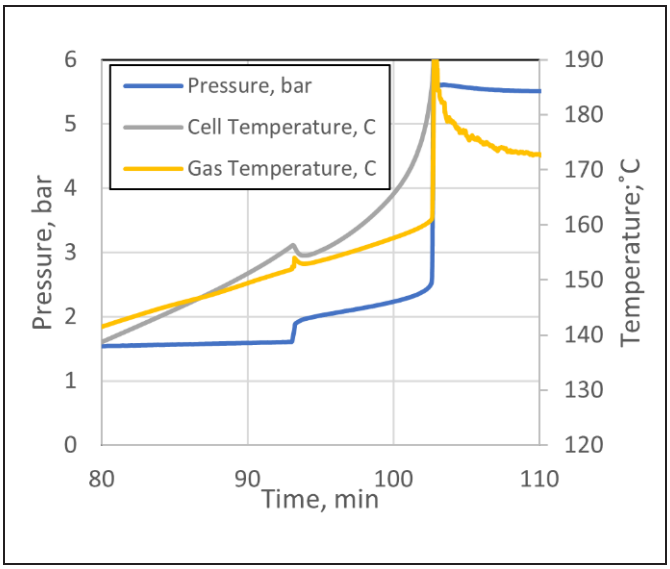

Figure 10. Pressure and temperature time plots of a single LTO in a 1,175-ml containera

The venting temperature of the cell normally occurred between 155 and 165 °C with an observed maximum of about 171 °C. Figure 9 demonstrates the accelerated temperature rise observed by the LTO cells during TR with observed maximum temperatures of the gases and cell surfaces of 265 °C and 450 °C, respectively.

In some instances, during TR, the thermocouple loses contact with the cell's surface and the recorded temperature reflects the gas temperature in the sealed container as opposed to the actual surface temperature of the cell. In all recorded data, the temperature never exceeded the autoignition temperature of methane at 600 °C.

Gas Generation

When the LIB's surface reaches a critical temperature, gas production from the cell begins, along with excess heat. A positive feedback loop grows at an exponential rate resulting in thermal runaway. This crucial temperature was found to be around 160 °C for these LTO cells. A venting event normally occurs at this temperature and a sudden release of gas enters the container. During this time, we see an increase in the pressure rate resulting from additional moles of gas and heat that are expelled into the container. In some instances, it is also possible to measure adiabatic cooling of the cell's surface temperature as shown in Figure 10, which depicts a snapshot of a single LTO cell in a 1,175-ml container.

As the cell continues to heat, releasing more gas and heat, the pressure in the canister increases rapidly until TR occurs. Utilizing the free volume of the sealed container and the ideal gas law, the moles of gas are computed as a function of heating time from the recorded gas temperature and pressure. An example of this is shown in a 1,175-ml container in Figure 11 where spikes in the pressure rate can be seen as moles of gas are released during the venting and thermal runaway events with the peak mole released occurring at the latter.

A slight drop in the moles can be seen and is likely due to the condensation of less volatile gases as the container and the gas begin to cool. The calculated moles were also used to estimate the volume of gasses released. The estimated equivalent volume of gases, which were considered to be at ambient temperature and pressure (22 °C and 1 bar), released by the cells was calculated by taking the volumes generated one minute after peak pressure and subtracting the amount calculated at the venting event. The resulting gas volumes were plotted against the amount of free space in the container as shown in Figure 12.

Researchers discovered that, as indicated in Figure 12, the amount of gas the LTO cells generated tended to rise with canister volume in agreement with Le Chatelier's principle to a maximum of 3.8 L for a single-cell and 11.0 L for the triple-cell configurations. An increase in volume results in a drop in pressure, which favors the side of the chemical reaction equilibrium with more moles. The triple-cell configuration also shows the expected volume of gas that would be anticipated. The average volume of vented gas, however, is slightly elevated at 3.4 L per cell compared to the 2.9 L per cell for tests in the single-cell configuration. Table 3 shows the average results compared to other past studies conducted in a similar configuration along with the volume of gasses released per their respective energy levels.

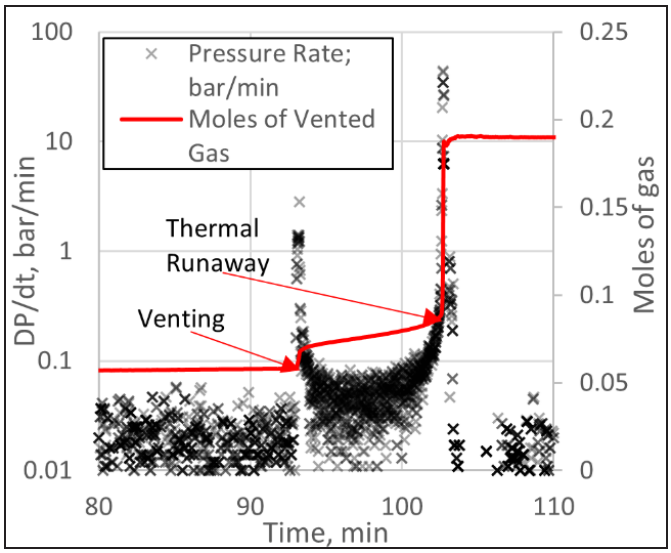

Figure 11. Time plot of pressure rates and moles of vented gas for a single LTO cell in a 1,175-ml container

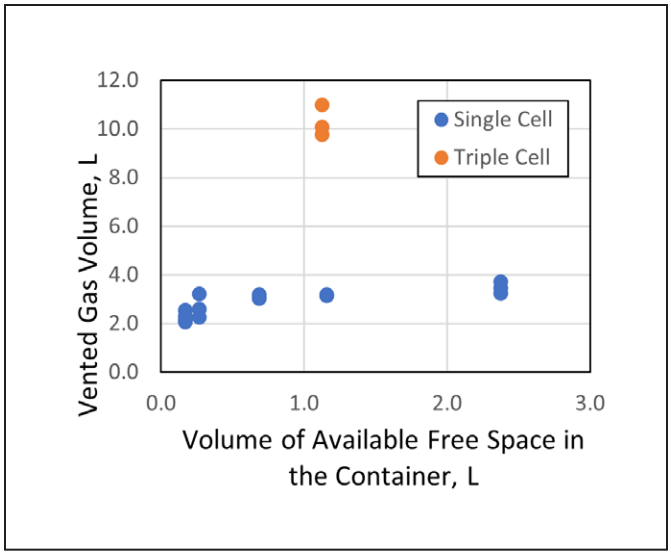

Figure 12. Volume of vented gases versus the available free space within the sealed container

In Table 3 we can see LTO releases a lesser amount of gas compared to the LFP 22650 type cell, but one must recognize this is a larger type of battery with a displacement volume nearly twice that of the LTO 18650. When accounting for the unit energy of each cell, the LTO has the highest amount of gases released, 0.94 L/Wh.

Thermal Runaway Pressures

Table 4 shows the results of maximum pressure measured during thermal runaway by the DATAQ in addition to the calculated ratio of free space to cell volume and the maximum pressure rise rates. All pressure measurements were absolute. Figure 13 has the same data plotted to show the inverse power relationship between the pressures observed and the free space to cell volume. The line at 9.62 bar corresponds to the 125-psig limit set for MSHA-approved XP enclosures. Using this line as a reference, one can determine that an available free space of about 40 times the volume of the LTO battery is needed to keep the pressures within the necessary specifications. However, it was only when the cells were placed in a 1,175 ml container that the pressure remained under the 9.62 bar limit for all the observations, which correlates to a free space per cell volume of 70.

Table 3. Summary of vented gas volumes

Cell type	Average Gas Volume, L	Average Gas Vol per Energy, L/Wh
LTO	2.9	0.94
NMC [14]	7.6	0.65
LFP [14]	4.4	0.36

Table 4. Summary of peak thermal runaway pressure

Free Space, mL	Free Space / Cell Vol	TR Pressure, bar	Max Dp/dt, bar/s
54.5	3.3	42.7	8.52
	3.3	39.2	5.98
	3.3	39.3	6.39
92.5	5.6	31.8	4.66
	5.6	32.0	4.25
	5.6	33.0	4.91
168.5	10.2	24.3	3.44
	10.2	23.9	3.34
	10.2	21.6	2.84
267.5	16.2	21.0	4.68
	16.2	17.9	2.85
	16.2	17.9	2.46
685.5	41.4	13.1	2.15
	41.4	10.8	1.20
	41.4	8.1	2.15
1158.5	70.0	5.3	0.51
	70.0	5.4	0.46
	70.0	5.6	0.56
2376.5	143.7	3.3	0.60
	143.7	3.5	0.23
	143.7	3.7	0.27
1125.4*	22.7*	14.7*	1.20*
	22.7*	14.9*	1.36*
	22.7*	14.8*	1.20*

*Triple-cell test

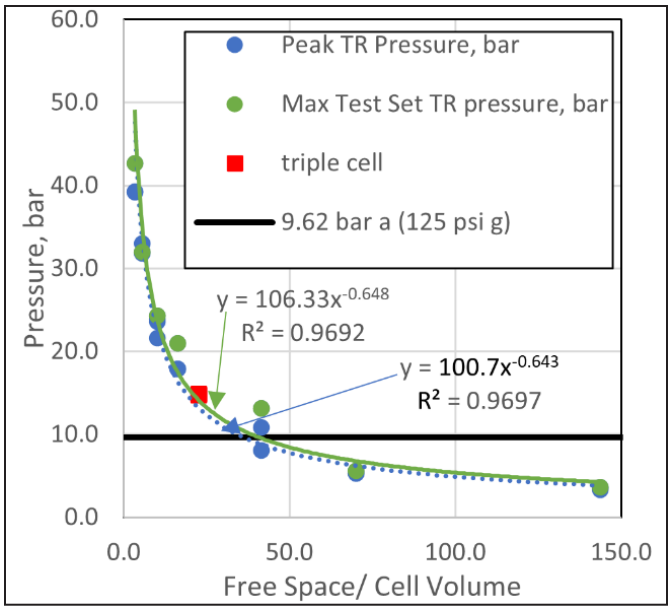

Figure 13. Pressure versus free space per cell volume for LTO type LIB in sealed containers

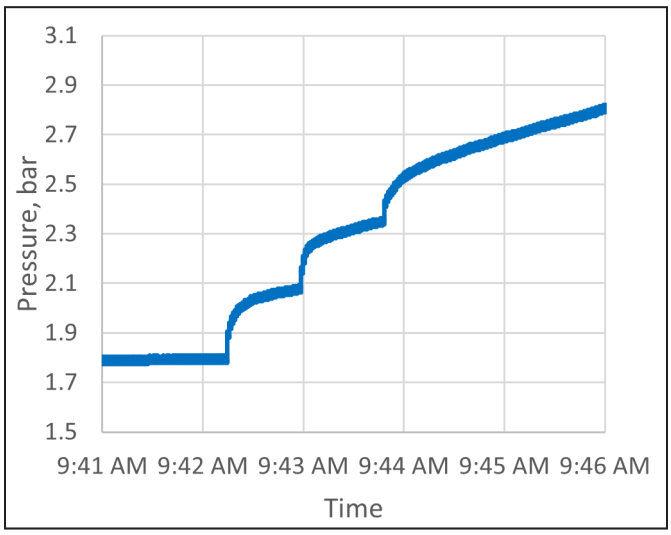

Figure 14. Triple-cell venting event in a 1,175-ml container showing additive pressures

Figure 14 shows one of the pressure-time plots where the venting of three cells was captured as distinct jumps in pressure.

Even though the volume of venting gas appeared higher for the three-cell configuration, the peak pressure seen in this configuration falls in line with the inverse power relationship as seen in Figure 13. In Figure 15 this new data for LTO-type batteries were compared to past NIOSH data looking at NMC-type and LFP-type cells.

Figure 15 shows how similar the LTO cells are to the LFP cells, and how much more reactive the NMC cells are.

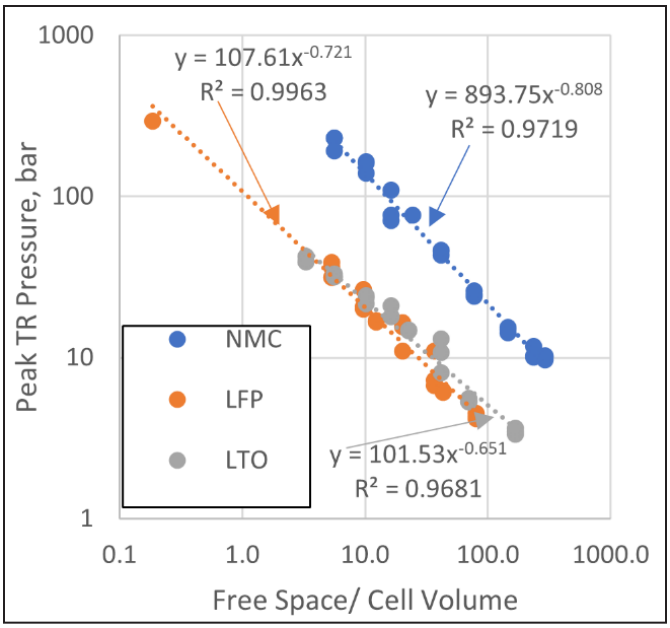

Figure 15. Comparison of peak thermal runway pressures from LTO, LFP [14], NMC [14] cells

Even though the LTO and LFP peak pressures look the same, the LFP-type batteries have a higher energy density which manufacturers will want to consider.

LIMITATIONS

The limitations of the study that need to be considered are as follows. The LTO cells were tested at a full state of charge. It is known that the thermal runaway severity is positively correlated with the state of charge [31]. Only one cell type from one manufacturer was used. There are other manufacturers that may use different cathode, separator, or electrolyte chemistries that fall under the category of LTO that were not tested. Differences in cell additives can influence failure response [32].

CONCLUSIONS

A very similar inverse power relationship was observed from the maximum thermal runaway pressures of LTO-type cells with the free space to cell volume ratio. This relationship of pressure to free space per cell volume most closely represented plots of an LFP-type cell. A container with an internal volume of 1,175 ml was necessary for a cell with a volume of 16.5 ml to meet the MSHA pressure generation threshold specification. The vented gases that were recorded during venting and thermal runaway were approximately 3 L per cell with a volume of 16.5 ml. Given the known energy density of the LTO cell, this results in the highest volume of gas per the energy of the cell. The temperatures recorded during thermal runaway were under

the normal temperatures for the autoignition of methane. These results should be taken into consideration during the selection of battery chemistry for use in BEVs in the mining environment.

DISCLAIMER

The findings and conclusions in this report are those of the authors and do not necessarily represent the official position of the National Institute for Occupational Safety and Health, Centers for Disease Control and Prevention. Mention of any company or product does not constitute endorsement by NIOSH.

REFERENCE

[1] The International Agency for Research on Cancer (2012). IARC: Diesel engine exhaust carcinogenic [Press Release No. 213]. World Health Organization. Retrieved August 2019 from www.iarc.fr/en/media-centre/pr/2012/pdfs/pr213_E.pdf.

[2] NIOSH (2017). Mining project: Advance strategies for controlling exposures to diesel aerosols. Cincinnati, OH: U.S. Department of Health and Human Services, Centers for Disease Control and Prevention, National Institute for Occupational Safety and Health. Retrieved September 2019 from www.cdc.gov/niosh/mining/researchprogram/projects/project_DieselAerosols.html.

[3] GMSG (2017). Recommended Practices for Battery Electric Vehicles in Underground Mining. 20160726_UG_Mining_BEV-GMSG-WG-v01-r01. Ormstown, QC, CA.

[4] Boston, W., Kowsmann, P. (2022) "Burning Electric-Vehicle Batteries Complicate Efforts to Fight Fire on Drifting Ship in Atlantic Ocean" Wall Street Journal from www.wsj.com/articles/burning-electric-vehicle-batteries-complicate-efforts-to-fight-fire-on-drifting-ship-in-atlantic-ocean-11645385571.

[5] Hummel, T.; Kar-Gupta, S.; Clarke, D. (2022). "Paris withdraws Bollore's electric buses after two catch fire." Reuters www.reuters.com/business/autos-transportation/paris-public-transport-network-suspends-bollore-e-buses-after-fire-incidents-2022-04-29/.

[6] Reasoner, J. J., Regier, B. A., Beckendorf, R., & McAllister, R. K. (2020). Update on the Risks of Electronic Cigarettes-Vaping. The Ochsner Journal, 20(1), 2–4. doi.org/10.31486/toj.20.0012.

[7] Gillett, S. (2021). Battery Electric Vehicle Emergency Response Incident Review and Best Practices. Workplace Safety North Virtual Symposium: Battery Electric Vehicle Safety in Mines, January 20, 2021. Retrieved August 2022 from www.workplacesafetynorth.ca/resources/virtual-symposium-battery-electric-vehicle-safety-mines.

[8] Jacques, D. (2019). BEV Pioneering Partnership at Borden—Celebrate the wins, face the challenges. Mining Diesel Emissions Council. MDEC 2019, October 7–10, Toronto, ON. S6P3. Retrieved August 2021 from mdec.ca/2019/S6P3_David_Jacques.pdf.

[9] Roth EP, Crafts CC, Doughty DH, McBreen J (2004) Advanced technology development program for lithium-ion batteries: Thermal abuse performance of 18650 Li-ion cells. Sandia Nat. Lab., Albuquerque Rep. SAND2004-0584, Retrieved August 2019 from pdfs.semanticscholar.org/7c66/2ecf8d3c4830c84283f225504e5b2f454ba8.pdf.

[10] Ponchaut, N., Marr, K., Colella, F., Somandepalli, V., Horn, Q. (2015). Thermal runaway and safety of large lithium-ion battery systems. In International Stationary Battery Conference, Orlando, FL.

[11] 30 CFR. (2018). Code of Federal Regulations, Mineral Resources, Parts 1 to 199, U.S. Department of Labor, Mine Safety and Health Administration, Arlington, VA, USA. Retrieved August 2022 from arlweb.msha.gov/regs/30cfr/.

[12] MSHA (2005). Requirements For Explosion Testing PER 30 CFR, 18.62, ASTP 2137. U.S. Department of Labor, Mine Safety and Health Administration, Arlington, VA, USA. Retrieved August 2021 from arlweb.msha.gov/TECHSUPP/ACC/StandardTestProcs/AS TP2137.pdf.

[13] Dubaniewicz, T.H., Zlochower, I., Barone, T., Thomas, R., Yuan, L. (2021). Thermal Runaway Pressures of Iron Phosphate Lithium-Ion Cells as a Function of Free Space Within Sealed Enclosures. Mining, Metallurgy & Exploration 38:539–547. doi.org/10.1007/s42461-020-00349-9.

[14] Dubaniewicz, T. H., Barone, T. L., Brown, C. B., Thomas, R. A. (2022). Comparison of thermal runaway pressures within sealed enclosures for nickel manganese cobalt and iron phosphate cathode lithium-ion cells. Journal of Loss Prevention in the Process Industries, 76, 104739. doi.org/10.1016/j.jlp.2022.104739.

[15] Yuan, L., Dubaniewicz, T., Zlochower, I., Thomas, R., Rayyan, N. (2020). Experimental study on thermal runaway and vented gases of lithium-ion cells. Process Safety and Environmental Protection, 144, 186–192.

[16] Barone, T. L., Dubaniewicz, T. H., Friend, S. A., Zlochower, I. A., Bugarski, A. D., Rayyan, N. S. (2021). Lithium-ion battery explosion aerosols: Morphology and elemental composition. Aerosol Science and Technology, 55(10), 1183–1201.

[17] Massé, R. C., C. Liu, Y. Li, L. Mai, and G. Cao (2017). Energy storage through intercalation reactions: Electrodes for rechargeable batteries. National Science Review 4 (1): 26–53.

[18] Nitta, N., F. Wu, J. T. Lee, and G. Yushin (2015). Li-ion battery materials: Present and future. Materials Today 18 (5):252–264.

[19] Sandhya, C.P., John, B. and Gouri, C. (2014). Lithium titanate as anode material for lithium-ion cells: a review. Ionics, 20(5), pp.601–620.

[20] Xia, H., Luo, Z. and Xie, J. (2014). Nanostructured lithium titanate and lithium titanate/carbon nanocomposite as anode materials for advanced lithium-ion batteries. Nanotechnology Reviews, 3(2), pp.161–175.

[21] Liu, W., Zhang, J., Wang, Q., Xie, X., Lou, Y. and Xia, B. (2014). The effects of Li2CO3 particle size on the properties of lithium titanate as anode material for lithium-ion batteries. Ionics, 20(11), pp.1553–1560.

[22] Rashid, M., Sahoo, A., Gupta, A. and Sharma, Y. (2018). Numerical modelling of transport limitations in lithium titanate anodes. Electrochimica Acta, 283, pp.313–326.

[23] Yi, J., Wang, C. and Xia, Y. (2013). Comparison of thermal stability between micro-and nano-sized materials for lithium-ion batteries. Electrochemistry communications, 33, pp.115–118.

[24] Kvasha, A., Gutiérrez, C., Osa, U., de Meatza, I., Blazquez, J.A., Macicior, H. and Urdampilleta, I. (2018). A comparative study of thermal runaway of commercial lithium ion cells. Energy, 159, pp.547–557.

[25] Reeves-McLaren, N., Hong, M., Alqurashi, H., Xue, L., Sharp, J., Rennie, A.J. and Boston, R. (2018). The Spinel LiCoMnO4: 5V Cathode and Conversion Anode. Energy Procedia, 151, pp.158–162.

[26] Chiba, K., Hamada, Y., Hayakawa, H., Hamao, N., Kataoka, K., Mamiya, M., Kijima, N., Ishida, N., Idemoto, Y. and Akimoto, J. (2019). A novel synthetic route of micrometer-sized $LiCoMnO_4$ as 5 V cathode material for advanced lithium ion batteries. Solid State Ionics, 333, pp.9–15.

[27] Ariyoshi, K., Yamamoto, H. and Yamada, Y. (2018). High dimensional stability of LiCoMnO4 as positive electrodes operating at high voltage for lithium-ion batteries with a long cycle life. Electrochimica Acta, 260, pp.498–503.

[28] Uyama, T., Inoue, T. and Mukai, K. (2018). Realizing the Ultimate Thermal Stability of a Lithium-Ion Battery Using Two Zero-Strain Insertion Materials. ACS Applied Energy Materials, 1(10), pp.5712–5717.

[29] Nestler, T., R. Schmid, W. Münchgesang, V. Bazhenov, J. Schilm, T. Leisegang, and D. C. Meyer (2014). Separators-technology review: Ceramic based separators for secondary batteries. American Institute of Physics Conference Proceedings 1597 (1):155–184.

[30] Duan, J., X. Tang, H. Dai, Y. Yang, W. Wu, X. Wei, and Y. Huang (2020). Building safe lithium-ion batteries for electric vehicles: A review. Electrochemical Energy Reviews 3:1–42.

[31] Golubkov, A., Scheikl, S., Planteu, R., Voitic, G., Wiltsche, H., Stangl, C., Fauler, G., Thaler, A., Hacker, V., (2015). Thermal runaway of commercial 18650 Li-ion batteries with LFP and NCA cathodes—impact of state of charge and overcharge. RSC Adv. 5, 57171–57186.

[32] Baird, A., Archibald, E., Marr, K., Ezekoye, O. (2020). Explosion hazards from lithium-ion battery vent gas. Journal of Power Sources. Volume 446, ISSN 0378-7753, doi.org/10.1016/j.jpowsour.2019.227257.

24-088

Underground Mine Ramp Design for Beginners

William G. Pariseau
University of Utah, Salt Lake City, Utah

INTRODUCTION

Safety of mine ramps begins with an analysis of stress that almost certainly must be done numerically to take into account ramp geometry, route geology, rock properties, and pre-ramp stresses. The popular finite element method serves analysis purposes quite well. As a practical matter several obstacles to implementation need to be addressed including collection of rock and joint properties along the proposed ramp route, selection of ramp type, and specification of cross-section shape, size, and route grade. Additionally, stresses along the proposed route must be specified, preferably from in situ measurements.

One need not be an expert in numerical methods to proceed to ramp design, although a background in mechanics of materials and rock mechanics is essential, and a first course in numerical methods is quite helpful. The necessary software is easily brought to the design task, more accurately, to the task of design evaluation. This software also addresses other important mine design problems including design of safe (1) main entries in stratified ground, (2) barrier pillars, (3) bleeder entries, (4) inter-panel barrier pillars, (5) room and pillar mines, (6) shafts, and (7) "tunnels" (Pariseau 2022).

PROBLEM DEFINITION

The problem is to compute displacements and related strains induced by ramp excavation and the stresses that result, given ramp geometry, geology including rock properties, and pre-ramp stress. The combination of pre-ramp stress and stress change induced by ramp excavation allows for computation of elastic and yielding zone extents about the ramp section and beyond. This information provides useful guidance to safe ramp design in the form of element safety factor distributions.

A local element safety factor concept defined as the ratio of strength to stress requires definitions of suitable measures of strengths and stress for analysis. Both arise in the context of stress-strain relations. Strength may be defined as stress at the elastic limit, so in case of the famous Mohr-Coulomb criterion one has $fs = \tau_m(\text{strength})/\tau_m(\text{stress})$ which reduces to $fs = C_o/\sigma_c$ in unconfined compression and to $fs = T_o/\sigma_t$ in uniaxial tension where C_o and T_o are unconfined compressive and tensile strengths, respectively. Here τ_m is the maximum shear stress at failure. Alternatively, $fs = J_2^{N/2}$ (strength)/τ_m (stress) where J_2 is the second invariant of deviatoric stress (a measure of shear strength) and N is an exponent determined by testing, usually between one and two. This alternative also reduces to the unconfined compression and tension cases and has the advantage of including the effect of the intermediate principal stress on strength. When the formation is isotropic and N=1, this definition reduces to the well-known Drucker-Prager criterion.

PROBLEM APPROACH

Approach to the problem is by the finite element method and is easy as one-two-three. Step one requires specification of rock properties in the region of interest including elastic moduli and strengths. An elastic response to an initial application load followed by inelastic behavior is illustrated in Figure 1.